Physics of Fluids

Drop impacting on a surface with adjustable wettability based on the dielectrowetting effect

Cite as: Phys. Fluids **32**, 097108 (2020); https://doi.org/10.1063/5.0023287
Submitted: 28 July 2020 . Accepted: 06 September 2020 . Published Online: 21 September 2020

Jiangen Zheng (郑建艮), Yang Cheng (成阳), Yingzhou Huang (黄映洲), Shuxia Wang (王蜀霞), Liyu Liu (刘雳宇), and Guo Chen (陈果)

Physics of Fluids ARTICLE scitation.org/journal/phf

Drop impacting on a surface with adjustable wettability based on the dielectrowetting effect

Cite as: Phys. Fluids 32, 097108 (2020); doi: 10.1063/5.0023287
Submitted: 28 July 2020 • Accepted: 6 September 2020 •
Published Online: 21 September 2020

Jiangen Zheng (郑建艮), Yang Cheng (成阳), Yingzhou Huang (黄映洲), Shuxia Wang (王蜀霞), Liyu Liu (刘雳宇), and Guo Chen (陈果)[a]

AFFILIATIONS

Chongqing Key Laboratory of Soft Condensed Matter Physics and Smart Materials, College of Physics, Chongqing University, Chongqing 400044, People's Republic of China

[a]Author to whom correspondence should be addressed: wezer@cqu.edu.cn

ABSTRACT

The dielectrowetting technique is an important method for controlling surface wettability. Herein, by combining the dielectrowetting technique with high-speed photography, the impact of a water drop on a surface with adjustable wettability is studied. Four different impact phenomena of the drop are identified, and the corresponding phase diagram is provided. As the surface wettability changes, the drop spreading factor and the dynamic contact angle differ for the same Weber number, exhibiting diverse drop behavior. A bubble entrapped on the surface is the most commonly observed phenomenon, and its maximum spreading factor and spreading time are dominated by the Weber number. However, its oscillation period and damping rate are independent of the Weber number. Moreover, a jet occurs on the surface with high hydrophobicity, and the inverse relationship between the jet velocity and radius is in good agreement with the theoretical model. Our work on drop impact based on the dielectrowetting effect can provide a new direction for the study of drop dynamics. Furthermore, the preparation method of the substrate with adjustable surface wettability could be applied in industrial fields such as inkjet printing and coating preparation.

I. INTRODUCTION

Drop impact is an important research topic in the field of fluid dynamics and a common phenomenon in nature as well as engineering. In nature, aerosols produced by rain splashes erode rocks.[1] In industry, the interaction between spray drops and a surface during spraying[2] and operation of equipment, such as inkjet printers[3] and high-power generators,[4] involves the drop impact phenomenon. Therefore, the systematic analysis of the drop impact mechanism and the determination of the key parameters affecting drop impact are important for the development of industrial manufacturing and technology.

Many factors affect drop impact, including fluid properties, such as impact velocity,[5] drop viscosity,[6] surface tension,[7] and substrate properties, such as wettability,[8] hardness,[9] roughness,[10] and temperature.[11] When a drop hits a smooth solid surface, the wettability of the substrate significantly affects the drop impact behavior, making it possible to control the drop impact behavior by adjusting the wettability of the substrate without changing other impact conditions. Currently, the common methods used to change the wettability of a substrate include treating the substrate with different surface energy materials[12] and preparing micro/nanostructures on the substrate.[13] For example, Lin *et al.*[14] obtained a hydrophobic substrate by silanizing silicon wafers with 1H,1H,2H,2H-perfluorodecyl-triethoxysilane and fabricated a superhydrophobic surface by depositing a fractal-like network of hydrophobized silica shells on clean glass slides.[15] However, the substrates prepared by these methods have a fixed wettability. Changing their wettability requires replacing the coating or changing the surface morphology and structure. The hardness and roughness of the substrates change accordingly. Thus, the corresponding experimental results cannot individually and objectively reflect the effect of surface wettability on drop impact.

Recent studies have shown that electrowetting[16–18] and dielectrowetting[19,20] techniques can effectively control the wettability of

a substrate. In electrowetting, a voltage is applied between a small electrode inserted into a conducting liquid drop and another electrode embedded in the substrate. A top electrode is required to maintain contact with the drop, rendering it difficult to adjust the surface wettability during drop impact. However, in dielectrowetting, interdigitated electrodes are usually fabricated and embedded in a solid surface to generate non-uniform electric fields. When the voltage is applied, the polarized dipoles in the dielectric liquid drop are attracted near the contact line and give rise to a Maxwell stress on the liquid–air interface, which must then decrease the curvature to reduce the Laplace pressure.[21] The dielectrowetting technique does not require a direct contact between the drop and electrodes, and it has been widely used to manipulate drops. For example, superdiffusion of drops[20] and drop transport, splitting, and merging[22] were realized on a dielectrowetting substrate induced by a non-uniform electric field. In addition, Wang *et al.*[23] adjusted the intensity and duration of the pulse voltage to control the spontaneous jumping height of the drops on a dielectrowetting superhydrophobic surface. Yang *et al.*[24] used a dielectrophoretic force to screen impact drops on a superhydrophobic surface. Their substrate adhesion can be reversed three times without losing the Cassie–Baxter state of the surface. Therefore, we used the dielectrowetting technique to reversibly adjust the wettability of the substrate, thus controlling the impact behavior of the drops on the prepared substrate while ensuring that the hardness and roughness of the substrate remain unchanged.

In this study, the dielectrowetting technique is used to quantitatively control the wettability of the substrate. The behavior of the drops after they impact substrates with different wettabilities is evaluated, and the underlying physics are further analyzed. First, we determine the phase diagram reflecting the relationship among the drop impact behavior, the Weber number (We), and the equilibrium contact angle by changing the impact height of the drop and surface wettability. Second, we focus on the most common phenomenon, a bubble entrapped on the surface, and discuss its spreading and oscillation processes. Third, we analyze the quantitative relationship between the Weber number and the maximum spreading factor, spreading time in the spreading stage, damping oscillation period, and damping rate in the oscillation stage. Finally, we summarize the occurrence condition of the jet and compare the relationship between the radius and velocity of the jet drop.

II. EXPERIMENTAL METHODS AND MATERIALS

Figure 1(a) shows a schematic of the experimental setup. The substrate was connected to a high-voltage direct current (DC) power supply (Dongwen DW-P503-1ACDF0, China) and fixed on the lifting stage. Figures 1(b) and 1(c) show the details of drop collision with the dielectrowetting substrate from two different perspectives. The initial diameter of the drop was D_0, and the impact velocity was v_0. An indium tin oxide (ITO) film was deposited on a glass substrate by magnetron sputtering, and parallel planar interdigital electrodes were fabricated by laser etching. The final morphology of the electrodes is shown in Fig. 1(c). The two sets of parallel planar interdigital electrodes were alternately arranged, and both the width of each electrode and the gap between two adjacent electrodes were d = 200 μm. To induce the dielectrowetting effect, we connected these two groups of electrodes to the ground terminal (marked in black) and the high-voltage output terminal (marked in red) of the high-voltage DC power supply. The voltage value varied from 0 V to 510 V in the experiment, and the dielectric layer may be damaged if the voltage is too high. Because the polydimethylsiloxane (PDMS, SYLGARD 184, America) film exhibits good insulation and hydrophobicity, it was used as a dielectric layer and hydrophobic layer in this experiment. To create a thin film of PDMS, we diluted the PDMS prepolymer with n-hexane. The PDMS prepolymer was composed of three components: main agent, auxiliary agent (crosslinker), and *n*-hexane (diluent) mixed in a mass ratio of 10:1:2. First, the prepolymer was fully stirred, and the internal bubbles were removed by vacuum degassing. Then, the PDMS film was prepared with a spin coater (KW-4A, China) at a speed of 5000 rpm. Finally, the substrate with the PDMS film was cured in a drying oven at 70 °C for 2 h. The thickness of the PDMS film was ~10 μm, and the contact angle of the stationary drops on the substrate surface was 117° ± 1°.

The liquid used in the experiment was ultra-pure water, and the ambient temperature was 23 °C. The surface tension, density, and dynamic viscosity of the liquid at this temperature were 72.8 mN/m, 1000 kg/m^3, and 1 mPa s, respectively. The drops were released through a needle connected to an injection pump (Longer Pump LSP01-2A, China) with an outer diameter of 0.64 mm and an inner diameter of 0.06 mm at a flow rate of 10 μl/min. The initial diameter of the drop (D_0) was 2.7 ± 0.1 mm. When the drops fell freely from different heights above the substrate, the impact velocity varied from 0.23 m/s to 3.19 m/s, and the corresponding Weber number

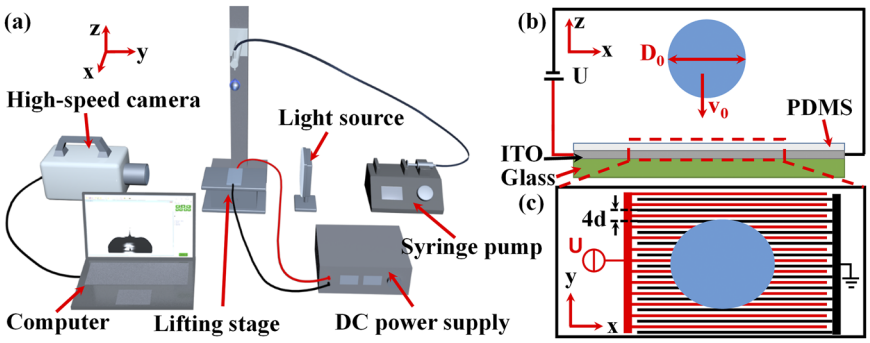

FIG. 1. (a) Overall experimental setup. (b) Schematic image of a drop impacting a dielectrowetting substrate that consists of ITO parallel planar interdigital electrodes and a thin PDMS dielectric layer; the substrate is connected to a high-voltage DC power supply to control the substrate wettability (xz perspective). (c) Morphology of the parallel planar interdigital electrodes with uniform spacing and width (xy perspective).

$\left(\mathrm{We} = \frac{\rho v_0^2 D_0}{\sigma}\right)$ and Reynolds number $\left(\mathrm{Re} = \frac{\rho v_0 D_0}{\mu}\right)$ ranged from 2.03 to 376.54 and 631.53 to 8603.01, respectively. The experimental videos were recorded at a rate of 5000 fps using a high-speed camera (Phantom V7.3, America) from the xz perspective. The spreading range of drop is quite different at varied impacting speed. To ensure the best display of the drop on the field of view and to facilitate subsequent quantitative data analysis, we used different lenses for slow and fast impacting drops. For the low-speed drop impact experiments, the high-speed camera was equipped with a 5× lens (M plan Apo 5×, Japan) with a resolution of 800 × 600 pixels^2, and the uncertainty of the measurements was 0.0078 mm/pixel. For the high-speed drop impact experiments, the high-speed camera was equipped with a Nikon Lens (AF-S micro Nikon 105 mm, China) with a resolution of 800 × 400 pixels^2, and the uncertainty of the measurements was 0.0148 mm/pixel. We defined θ_{eq} as the equilibrium contact angle of the static drops parallel to the electrode in this work. We obtained the dynamic contact angle (θ), contact diameter (D), and middle height (H) of the drop from the videos for subsequent analysis using the MATLAB (MathWorks, Inc., USA) algorithm. The actual impact velocity was obtained by the movement of the drops' center of gravity before contact with the substrate. All experiments were repeated under identical conditions for a minimum of three times to ensure the repeatability and accuracy of the results.

III. RESULTS AND DISCUSSION

First, we confirmed the effectiveness of the dielectrowetting substrate and observed the corresponding responses of the drop on the substrate when different voltages were applied. When a drop with a diameter smaller than the capillary length rested on the dielectrowetting substrate, the degree of wetting was determined by the local minimum value of the surface energy generated at the solid–vapor (σ_{sv}), solid–liquid (σ_{sl}), and liquid–vapor (σ_{lv}) interfaces. The drop initially formed a spherical cap because of these three interfacial tensions. Multiple nonuniform electric fields were generated when the voltage was applied owing to the geometric arrangement of the electrodes. The induced dielectrophoresis parallel to the electrode direction (x-axis direction) generated stress along the liquid interface near the three-phase contact line, pushing the liquid to spread along the direction parallel to the electrode. Concurrently, the contact angle of the drop decreased with increasing applied voltage. However, the dielectrophoresis perpendicular to the direction of the electrode (y-axis direction) generated an energy barrier because of the periodical arrangement of the electrodes, preventing the movement of the contact line in this direction. It should be noted that the asymmetric electric field effect played a role in static drop situation and in the retraction stage of impacting drop. However, no observable asymmetric spreading was found for the impacting drop measurements in this work since the spreading process of drop was dominated by its inertial force. Therefore, we focused on the response of the drop parallel to the electrode. Figure 2 shows the variation in the equilibrium contact angle of the drops under different voltages. The equilibrium contact angle measurements at each voltage were repeated three times, and the error bar in Fig. 2 illustrates the corresponding standard deviation of each data point. With increasing applied voltage, the equilibrium contact angles of the left and right sides of the drop continuously decreased.

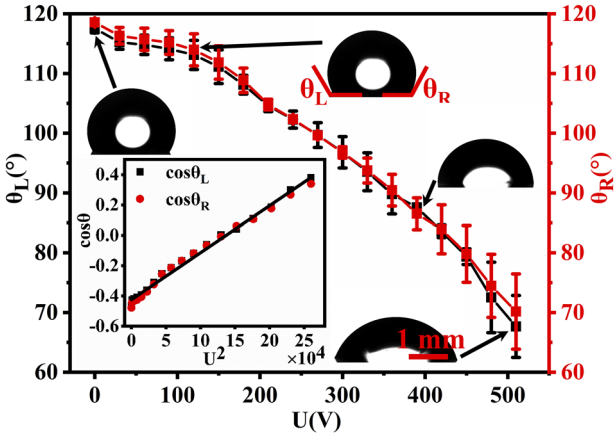

FIG. 2. Variation in the equilibrium contact angle (θ_L) on the left side and equilibrium contact angle (θ_R) on the right side of the drop with the applied voltage U. The morphologies of the drop on the dielectrowetting substrate at four different voltage values, 0 V, 120 V, 390 V, and 510 V, are shown. (Inset) Relationship between the cosine of the contact angle and square of the voltage, and the solid line is the fitting line. The scale bar is 1 mm.

The morphologies of the drop under four different applied voltages are also illustrated. The inset in Fig. 2 shows that the cosine value of the equilibrium contact angle changes with the square of the voltage. The relationship between the change in the equilibrium contact angle parallel to the electrode and the applied voltage of the stretched drops on the dielectrowetting substrate satisfies the Young–Lippmann equation,[19]

$$\cos\theta_{eq}(U) - \cos\theta_0 = \frac{\varepsilon_0(\varepsilon_l - 1)}{2\sigma_{LV}\delta}U^2, \tag{1}$$

where $\theta_{eq}(U)$ is the equilibrium contact angle of the drop parallel to the electrode under different voltages, θ_0 is the equilibrium contact angle without voltage, and $\varepsilon_0 = 8.85 \times 10^{-12}$ F/m and $\varepsilon_l = 80$ are the dielectric constant of the vacuum and liquid, respectively. The cosine value of the equilibrium contact angle is proportional to the square of the voltage, which satisfies the relationship of Eq. (1) and confirms the effectiveness of the dielectrowetting substrate.

When a drop impacts a solid surface with varied wettability, different phenomena may occur because of the dynamic interaction between the liquid drop and solid surface. The equilibrium contact angle of the drop on the surface of the dielectrowetting substrate can be controlled by adjusting the voltage, and the Weber number of the drop is determined by its actual impacting velocity. Thus, we obtained the phase diagram of the drops impacting the dielectrowetting substrate with different wettabilities, as shown in Fig. 3. Four different phenomena were observed on the dielectrowetting substrate: deposition, bubble entrapped on the surface, the jet, and bubble entrapped in the drop. The deposition phenomenon appeared between a low Weber number (We < 3.6) and a high Weber number (We > 294.06); however, the bubble entrapped on the surface occurred over a wide range of Weber numbers (3.6 ≤ We ≤ 294.06). Three phenomena, bubble entrapped on the surface, the jet, and bubble entrapped in the drop, occurred within a moderate Weber number range (9.53 ≤ We ≤ 20.35). Figure 3 shows that the drop

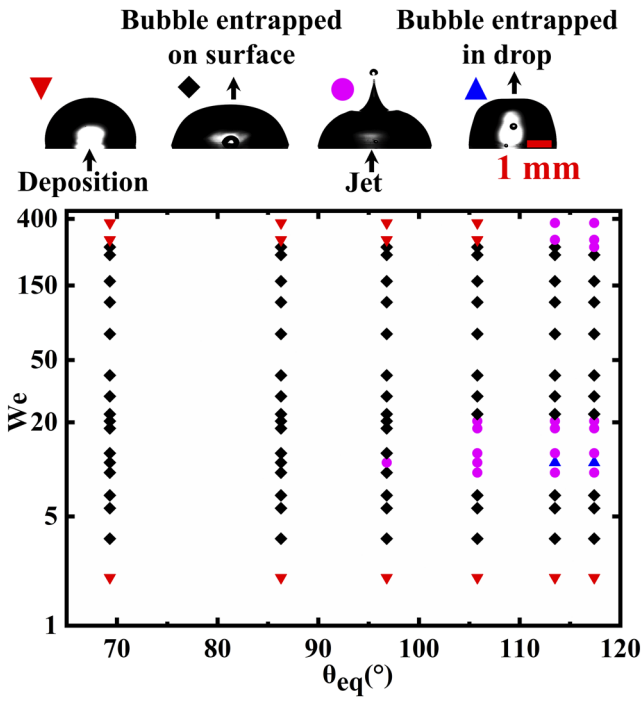

FIG. 3. Phase diagram of the drops impacting the dielectrowetting substrate with different equilibrium contact angles. The relationship among the impact behavior of the drops, Weber number, and wettability of the substrate is illustrated.

behaviors varied with different Weber numbers at the same wettability, possibly caused by the competition between inertial force and surface tension. The jet is more likely to appear at a higher inertial energy situation, while deposition prefers to occur when the surface tension dominates. Furthermore, different drop behaviors were also observed at the same Weber number with the change in surface wettability. When a drop hits a lower wettability surface, its spreading distance and energy dissipation during spreading are weaker, resulting in a higher retraction energy, which may be conducive to the formation of the jet or bubble.

At We = 11.05, three phenomena—bubble entrapped in the drop, the jet, and bubble entrapped on the surface—occurred in succession, and an increase in surface wettability was reflected through the decrease in the equilibrium contact angle of the drop. Figures 4(a)–4(c) show the high-speed images of these three phenomena at three typical equilibrium contact angles, θ_{eq} = 117.4°, 96.8°, and, 69.3°, respectively. The moment when the drop contacted the surface was considered as time zero in all our measurements. Comparing these three phenomena, from 0 ms to 5.4 ms, the drop morphology was almost the same; however, after 5.4 ms, the drop exhibited different behaviors. At θ_{eq} = 117.4°, a bubble was entrapped inside the drop after impact. However, at θ_{eq} = 96.8° and 69.3°, the jet and bubble entrapped on the surface, respectively. In this set of experiments, the Weber number of the drops remained the same, and the hardness and roughness of the substrate did not change. The only difference was the change in the equilibrium contact angle of the surface caused by the dielectrowetting effect. Two parameters were defined for the quantitative analysis: drop spreading factor β and drop dynamic contact angle θ; β is defined as β = D/D$_0$, where

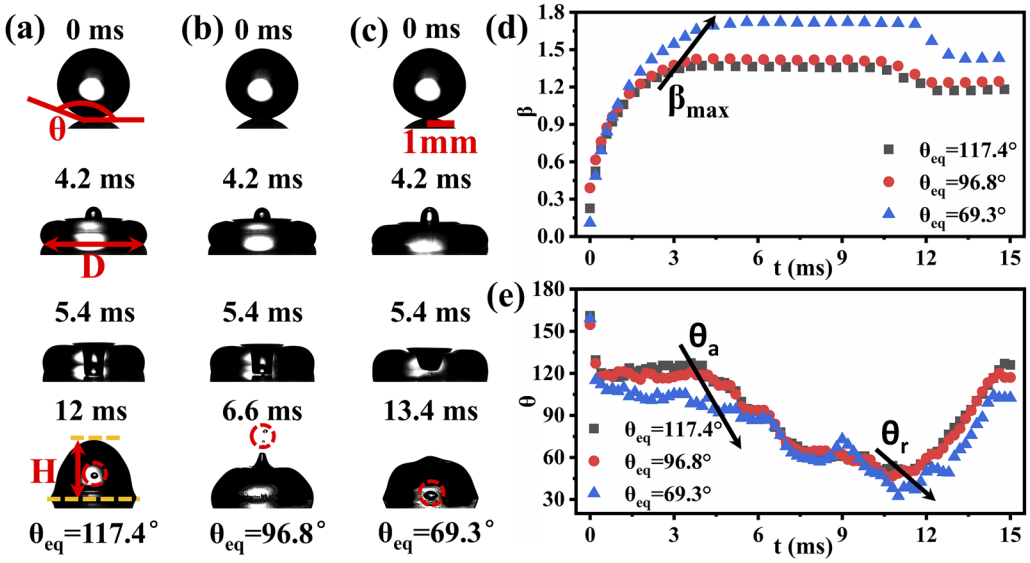

FIG. 4. Impact drops exhibit different behaviors at different surface wettabilities and the same Weber number (We = 11.05). For (a), θ_{eq} = 117.4°, a bubble is entrapped in the drop; for (b), θ_{eq} = 96.8°, jet appears; and for (c), θ_{eq} = 69.3°, a bubble is entrapped on the solid surface. (d) Plot of β (β = D/D$_0$) with time. The black arrow shows the trend of β_{max} with varied wettability. Panel (e) shows the corresponding dynamic contact angle θ under different wettabilities; θ_a and θ_r are the advancing and receding angles of the drops on the substrate, respectively. The scale bar represents 1 mm.

D is the spreading diameter of the drop on the surface. Figure 4(d) shows the time-varying curve of β. As the drop spread, β gradually increased and reached its maximum, β_{max}, which lasted for several milliseconds until the drop began to retract. At this time node, the contact angle of the drop changed from advancing contact angle θ_a to receding contact angle θ_r. The β values at these three wetting states were almost the same for the first 1.5 ms. However, as the equilibrium contact angle decreased, the value of β_{max} increased, and the time to reach β_{max} also increased, as indicated by the black arrow in Fig. 4(d). Figure 4(e) shows the dynamic contact angle of the drop on the surface. When a drop spread, its β increased; however, the drop maintained its θ_a. When β_{max} remained unchanged, the transition from drop spreading to receding occurred. During this transition period, the dynamic contact angle of the drop gradually decreased and changed from θ_a to θ_r. Both θ_a and θ_r decreased as the wettability increased, as demonstrated by the black arrows in Fig. 4(e). Comparing the data, the β of the two phenomena of the bubble entrapped in the drop and jet was almost the same. The difference in phenomena was caused by the difference in the dynamic contact angle. However, the phenomenon of the bubble entrapped on the surface occurred at a higher applied voltage. In this case, the stronger dielectrophoretic force increased β_{max} and θ_a and θ_r decreased. Therefore, it is possible to accurately control the phenomenon after the drop impacts the same substrate by changing the equilibrium contact angle of the substrate through the dielectrowetting effect, while the other conditions remained constant.

In this study, the bubble entrapped on the surface was most commonly observed at the Weber number intervals of $3.6 \le We \le 6.82$ and $22.55 \le We \le 294.06$. Figure 5(a) shows the β value of the drop with time at We = 6.82 and $\theta_{eq} = 117.4°$. Figure 5(b) shows the change in the dimensionless mid-height H/D_0 during the oscillation of the drop from 100 ms. Under the experimental conditions in this work, three stages typically occurred for the impacting drop: spreading, retraction, and oscillation. When the drop hit the surface, its contact front initially advanced quickly and only decelerated when the drop began to approach its maximum spreading position. The moment when the drop reached its maximum spreading distance was defined as t_s. Therefore, β reached its maximum value at $t = t_s$, as shown in Fig. 5(a). Then, the drop maintained β_{max} until the three-phase contact line of the drop began to retract. In this process, the contact angle of the drop continuously decreased from a higher θ_a to a lower θ_r. Then, the three-phase contact line began to contract, and the β value was reduced. Finally, after a period of retraction, the drop entered the oscillating stage. During this stage, the β value remained almost unchanged. Thus, the drop made a fixed three-phase contact line surface wave oscillation motion until the internal energy was completely dissipated to reach the final equilibrium state. At the beginning of oscillation, the inertial force, viscous force, and surface tension all played important roles. As time passed, the role of the surface tension became dominant, and the middle height of the drop was chosen after 100 ms for quantitatively analyzing the measurements. The damped oscillation curve is shown in Fig. 5(b) and is fitted by a damped sine function as follows:

$$H/D_0 = H_{eq}/D_0 + A \cdot e^{-\gamma t} \sin\left(2\pi \frac{t}{T} + \varphi\right), \tag{2}$$

where φ is the phase; H_{eq} is the middle height after the drop reached the equilibrium state; and A, γ, and T are the amplitude, damping rate, and period of the drop oscillation, respectively. The fitted values agreed with the experimental data values, as shown by the coincidence of the red solid line and black solid line in Fig. 5(b). In addition, the inset in Fig. 5(b) shows the disorder after fitting, and the residual is relatively small, which confirms that only one oscillation mode is excited in our case.[25]

A recent study replaced θ_a in the previous model with the average value of the apparent dynamic contact angle of the drop during the spreading stage, which is referred to as the plateau contact angle θ_d, to obtain a new theoretical expression of β_{max},[26]

$$(We + 12)\beta_{max} = 8 + \beta_{max}^3\left(3(1 - \cos\theta_d) + 4\frac{We}{\sqrt{Re}}\right). \tag{3}$$

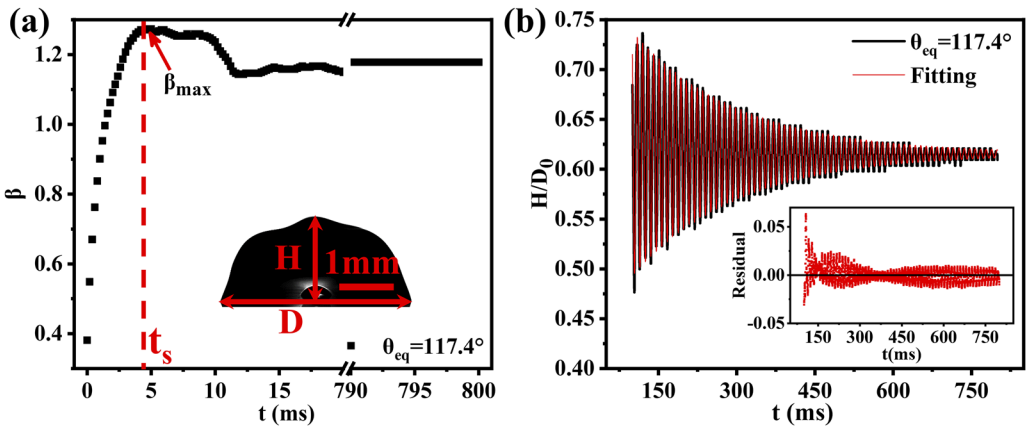

FIG. 5. (a) Drop spreading factor β at We = 6.82 and $\theta_{eq} = 117.4°$; β reaches its maximum value β_{max} at $t = t_s$. (b) Variation in dimensionless middle height H/D_0 during drop oscillation. The black line represents the experimental data, and the red line is the fitting values obtained by the damping sine function. (Inset) The residual curve of H/D_0 after fitting.

Figure 6(a) shows the relationship between β_{max} and Weber number under different wettability conditions. The red line is the fitting result of the experimental data $\beta_{max} \propto We^{0.27}$, which is similar to the theoretical curve ($\beta_{max} \propto We^{0.25}$) illustrated by the black line. In addition, the wettability of the substrate surface had a minimal effect on β_{max} of the drop on the dielectrowetting substrate at the same Weber number because the influence of the wettability of the substrate was low in the spreading stage after the drop impacted the substrate. The flow of the liquid in the diffusion layer was dominated by inertia.[27] The wettability of the substrate becomes important only when the velocity of the liquid layer is low because adhesion is initiated. Therefore, at the same Weber number, the small difference in β_{max} was attributed to the wettability of the drops on the dielectrowetting substrate. The smaller the equilibrium contact angle of the drops on the surface of the substrate, the larger the β_{max}. Further comparison shows that all the experimental values were lower than the theoretical ones because the actual energy dissipation was larger than that in the ideal case. In addition, although the vapor–liquid interface of the drop stopped moving at the maximum spreading diameter, there was an inertial flow inside the drop, which could also lead to overestimation.[28]

Spreading time t_s has already been defined as the time interval from the moment the drop touched the surface to the moment it reached the maximum spreading diameter. We modified the capillary-inertia time (t_i) by replacing the initial drop radius R_0 with the maximum spreading radius R_{max} and obtained the following: $t_i = (\rho R_{max}/\sigma)^{0.5}$. The experimental data collapse to a master curve in the log–log plot of the normalized spreading time t_s as a function of We [Fig. 6(b)]. Therefore, in our work, the general scaling law of t_s was $t_s/t_i = 1.57We^{-0.58}$.

Figure 6(c) shows the oscillation period (T) at various Weber numbers. Here, T was almost constant under all experimental conditions. The capillary number is represented by Ca = $\frac{\mu v_0}{\sigma}$, where $\mu = 1 \times 10^{-3}$ mPa s and $\sigma = 72.8 \times 10^{-3}$ N/m are the viscosity and surface tension of the liquid, respectively, and the impact velocity for the case of the drop entrapped on the surface ranged from 0.31 m/s to 3.19 m/s. Using these typical values, the calculated Ca number ranged from 0.0043 to 0.044, indicating that the oscillation process was dominated by the surface energy. Therefore, T can be related to the inertial-capillary time scale (τ_c), which is defined as $\tau_c = \sqrt{\frac{\rho D_0^3}{8\sigma}}$, where ρ is the liquid density and τ_c is a constant number in this

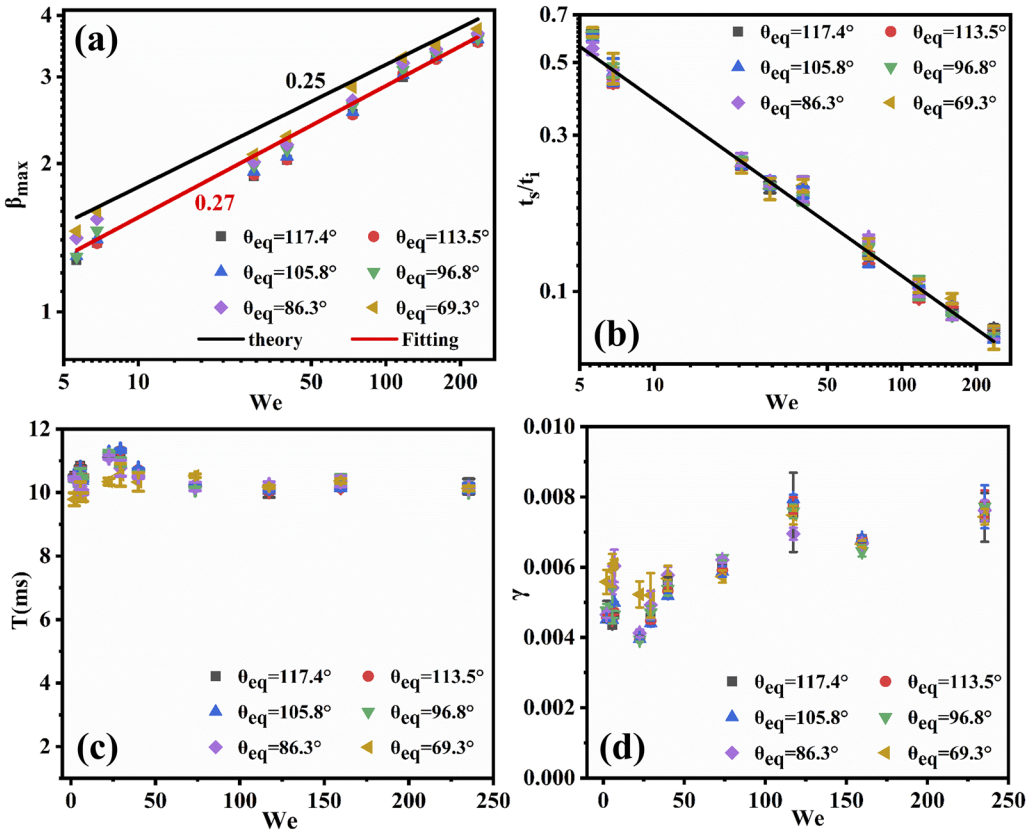

FIG. 6. (a) Log–log plot of the maximum spreading factor (β_{max}) as a function of the Weber number at different wettabilities. The red line is the fitting line obtained from the experimental data, and the black line is the result obtained from the theoretical analysis. (b) Log–log plot of the normalized spreading time t_s using the modified capillary-inertia time as a function of We. (c) Drop oscillation period as a function of the Weber number. (d) Drop oscillation damping rate γ as a function of We.

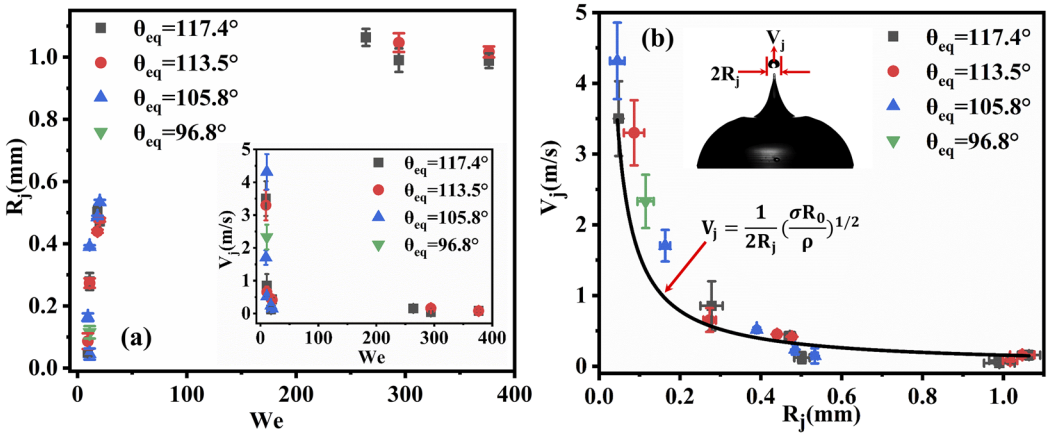

FIG. 7. (a) Radius of the jet drop R_j as a function of the Weber number We. (Inset) Velocity of the jet drop V_j as a function of We. (b) Relationship between V_j and R_j. (Inset) The corresponding parameter description. The black line is the plot of the theoretical fitting.

study. This was consistent with our oscillation period results, and we obtained $T = \pi/\sqrt{3}\tau_c$ by adding an appropriate coefficient. Figure 6(d) shows the variation in the drop oscillation damping rate (γ) with We. In this study, γ ranged from 0.004 to 0.008. It was nearly independent of the Weber number of the impacting drop, which was consistent with the previously reported results.[14] In addition, γ increased with decreasing θ_{eq} under the same Weber number. Thus, the viscous damping was stronger on the substrate with a low equilibrium contact angle, possibly owing to the longer wavelengths of motion of the drop on a more hydrophilic surface.[29] Thus, considerable viscous energy dissipation was observed in each oscillation cycle. This difference was more pronounced at a low Weber number; however, the difference was reduced at high Weber numbers.

The jet occurred on the surface with higher hydrophobicity, as shown by the phase diagram in Fig. 3. According to previous studies, the collapse of the air cavity during drop recoiling triggers the formation of the jet, and it is usually observed when a drop hits a superhydrophobic surface at a low impact velocity (the We number is less than 6.1).[30,31] However, the minimum We number for jet formation was 9.53 in this work. This inconsistency may be due to the difference in the degree of surface hydrophobicity. The equilibrium contact angle of our surface did not exceed 120°, far from reaching a superhydrophobic state. Figure 7(a) shows the relationship between the radius of the jet drop (R_j) and Weber number under different surface wettability conditions. As can be seen, R_j increased sharply with an increase in the Weber number and reached a steady value of ~1 mm when the Weber number exceeded 250. The inset in Fig. 7(a) shows the velocity of the jet drop (V_j) at various Weber numbers. Initially, V_j decreased rapidly with an increase in the Weber number, reaching and maintaining a near-zero value at a high Weber number. Figure 7(b) shows the relationship between V_j and R_j. The jet velocity decreased with an increase in the jet radius. Bonn *et al.* obtained a relationship between the velocity and radius of the jet drop based on energy conservation as follows:

$$V_j \approx \frac{1}{2R_j}\left(\frac{\sigma R_0}{\rho}\right)^{1/2}. \quad (4)$$

All experimental data under different wettability conditions showed good agreement with this relationship, as indicated by the black line in Fig. 7(b).

IV. CONCLUSIONS

This study proposed a method of controlling the equilibrium contact angle of a drop on a surface on the basis of the dielectrowetting effect to achieve quantitative control of the surface wettability, and the drop impact on this wettability adjustable surface was studied. Four different drop impact phenomena were classified in the experiment: deposition, bubble entrapped in the drop, the jet, and bubble entrapped on the surface. The corresponding phase diagram was summarized. With the change in surface wettability, the spreading factor and dynamic contact angle of the drop were different; therefore, the drops showed diverse behavior even at the same Weber number. For the most common phenomenon, i.e., a bubble entrapped on the surface, its maximum spreading factor and spreading time were dominated by the Weber number; however, there was minimal correlation with surface wettability. Further analysis revealed that the oscillation period and damping rate were independent of the Weber number. In addition, jet appeared on the surface with higher hydrophobicity, and the inverse relationship between the jet velocity and radius was discussed. This research on drop impact based on the dielectrowetting effect provides a new direction for the study of drop dynamics. Moreover, the preparation scheme of the surface with adjustable surface wettability could be applied in industrial fields such as inkjet printing and coating preparation.

ACKNOWLEDGMENTS

This work was supported by the National Natural Science Foundation of China (Grant Nos. 11604030 and 11674043) and the Natural Science Foundation Project of CQ CSTC (Grant No. cstc2020jcyj-msxmX0106), and the Fundamental Research Funds for the Central Universities (2020CDJ-LHSS-002). We would also

like to thank Analytical and Testing Center of Chongqing University for imaging service.

There are no conflicts of interest to declare.

DATA AVAILABILITY

The data that support the findings of this study are available from the corresponding author upon reasonable request.

REFERENCES

[1]Y. S. Joung and C. R. Buie, "Aerosol generation by raindrop impact on soil," Nat. Commun. **6**, 6083 (2015).
[2]D. W. Stanton and C. J. Rutland, "Multi-dimensional modeling of thin liquid films and spray-wall interactions resulting from impinging sprays," Int. J. Heat Mass Transfer **41**(20), 3037–3054 (1998).
[3]B. Jiang, Y. D. Huang, and Y. P. Bai, "Noncontact and rapid analysis of the quality of the recording coating on ink jet printing by near-infrared spectroscopy," Analyst **136**(24), 5157–5161 (2011).
[4]W. Xu, H. Zheng, Y. Liu, X. Zhou, C. Zhang, Y. Song, X. Deng, M. Leung, Z. Yang, R. X. Xu, Z. L. Wang, X. C. Zeng, and Z. Wang, "A droplet-based electricity generator with high instantaneous power density," Nature **578**(7795), 392–396 (2020).
[5]S. Wildeman, C. W. Visser, C. Sun, and D. Lohse, "On the spreading of impacting drops," J. Fluid Mech. **805**, 636–655 (2016).
[6]A. Kumar and D. K. Mandal, "Impact of emulsion drops on a solid surface: The effect of viscosity," Phys. Fluids **31**(10), 102106 (2019).
[7]S. Baek, H. S. Moon, W. Kim, S. Jeon, and K. Yong, "Effect of liquid droplet surface tension on impact dynamics over hierarchical nanostructure surfaces," Nanoscale **10**(37), 17842–17851 (2018).
[8]H. Almohammadi and A. Amirfazli, "Droplet impact: Viscosity and wettability effects on splashing," J. Colloid Interface Sci. **553**, 22–30 (2019).
[9]L. Q. Chen, E. Bonaccurso, P. G. Deng, and H. B. Zhang, "Droplet impact on soft viscoelastic surfaces," Phys. Rev. E **94**(6), 063117 (2016).
[10]C. Lv, P. Hao, X. Zhang, and F. He, "Drop impact upon superhydrophobic surfaces with regular and hierarchical roughness," Appl. Phys. Lett. **108**(14), 141602 (2016).
[11]A. Sreenivasan and S. Deivandren, "Splashing of fuel drops impacting on heated solid surfaces," Phys. Fluids **32**(3), 032104 (2020).
[12]A. J. Meuler, J. D. Smith, K. K. Varanasi, J. M. Mabry, G. H. McKinley, and R. E. Cohen, "Relationships between water wettability and ice adhesion," ACS Appl. Mater. Interfaces **2**(11), 3100–3110 (2010).
[13]T. L. Liu and C.-J. C. Kim, "Turning a surface superrepellent even to completely wetting liquids," Science **346**(6213), 1096–1100 (2014).
[14]S. Lin, B. Zhao, S. Zou, J. Guo, Z. Wei, and L. Chen, "Impact of viscous droplets on different wettable surfaces: Impact phenomena, the maximum spreading factor, spreading time and post-impact oscillation," J. Colloid Interface Sci. **516**, 86–97 (2018).
[15]X. Deng, L. Mammen, H.-J. Butt, and D. Vollmer, "Candle soot as a template for a transparent robust superamphiphobic coating," Science **335**(6064), 67–70 (2012).
[16]K. X. Zhang, Z. Li, and S. Chen, "Analytical prediction of electrowetting-induced jumping motion for droplets on hydrophobic substrates," Phys. Fluids **31**(8), 081703 (2019).
[17]Q. Vo and T. Tran, "Contact line friction of electrowetting actuated viscous droplets," Phys. Rev. E **97**(6), 063101 (2018).
[18]Y. Guan, M. N. Zhu, B. Y. Li, J. Y. Tu, L. Xing, and X. Y. Chen, "Numerical investigation of continuous droplet transport in parallel-plate electrowetting-on-dielectric digital microfluidics (EWOD DMF) with stripped electrodes," Phys. Fluids **32**(1), 012010 (2020).
[19]G. McHale, C. V. Brown, M. I. Newton, G. G. Wells, and N. Sampara, "Dielectrowetting driven spreading of droplets," Phys. Rev. Lett. **107**(18), 186101 (2011).
[20]G. McHale, C. V. Brown, and N. Sampara, "Voltage-induced spreading and superspreading of liquids," Nat. Commun. **4**, 1605 (2013).
[21]A. M. J. Edwards, C. V. Brown, M. I. Newton, and G. Mchale, "Dielectrowetting: The past, present and future," Curr. Opin. Colloid Interface Sci. **36**, 28–36 (2018).
[22]H. Geng, J. Feng, L. M. Stabryla, and S. K. Cho, "Dielectrowetting manipulation for digital microfluidics: Creating, transporting, splitting, and merging of droplets," Lab Chip **17**(6), 1060–1068 (2017).
[23]Z. Wang, D. van den Ende, A. Pit, R. Lagraauw, D. Wijnperlé, and F. Mugele, "Jumping drops on hydrophobic surfaces, controlling energy transfer by timed electric actuation," Soft Matter **13**(28), 4856–4863 (2017).
[24]J. Yang, D. Wang, H. Liu, L. Li, L. Chen, H.-R. Jiang, and X. Deng, "An electric-field-dependent drop selector," Lab Chip **19**(7), 1296–1304 (2019).
[25]J. Zheng, H. Shi, G. Chen, Y. Huang, H. Wei, S. Wang, and W. Wen, "Relaxation of liquid bridge after droplets coalescence," AIP Adv. **6**(11), 115115 (2016).
[26]D. C. Vadillo, A. Soucemarianadin, C. Delattre, and D. C. D. Roux, "Dynamic contact angle effects onto the maximum drop impact spreading on solid surfaces," Phys. Fluids **21**(12), 122002 (2009).
[27]M. Marengo, C. Antonini, I. V. Roisman, and C. Tropea, "Drop collisions with simple and complex surfaces," Curr. Opin. Colloid Sci. **16**(4), 292–302 (2011).
[28]C. Clanet, C. Béguin, D. Richard, and D. Quéré, "Maximal deformation of an impacting drop," J. Fluid Mech. **517**, 199–208 (2004).
[29]D. Banks, C. Ajawara, R. Sanchez, H. Surti, and G. Aguilar, "Effects of liquid and surface characteristics on oscillation behavior of droplets upon impact," Atomization Spray **24**(10), 895–913 (2014).
[30]D. Bartolo, C. Josserand, and D. Bonn, "Singular jets and bubbles in drop impact," Phys. Rev. Lett. **96**(12), 124501 (2006).
[31]L. Chen, L. Li, Z. Li, and K. Zhang, "Submillimeter-sized bubble entrapment and a high-speed jet emission during droplet impact on solid surfaces," Langmuir **33**(29), 7225–7230 (2017).